Role of square planar coordination in the magnetic properties of Na$_4$IrO$_4$

Xing Ming,[1,2] Carmine Autieri,[2] Kunihiko Yamauchi,[3] and Silvia Picozzi[2,*]

[1]*College of Science, Guilin University of Technology, Guilin 541004, People's Republic of China*
[2]*Consiglio Nazionale delle Ricerche CNR-SPIN, UOS L'Aquila, Sede Temporanea di Chieti, 66100 Chieti, Italy*
[3]*ISIR-SANKEN, Osaka University, 8-1 Mihogaoka, Ibaraki, Osaka, 567-0047, Japan*

Iridates supply fertile ground for unconventional phenomena and exotic electronic phases. With respect to well-studied octahedrally coordinated iridates, we focus our attention on a rather unexplored iridate, Na$_4$IrO$_4$, showing an unusual square planar coordination. The latter is key to rationalizing the electronic structure and magnetic property of Na$_4$IrO$_4$, which is here explored by first-principles density functional theory calculations and Monte Carlo simulations. Due to the uncommon square planar crystal field, Ir $5d$ states adopt an intermediate-spin state with double occupation of the d_{z^2} orbital, leading to a sizable local spin moment, at variance with many other iridates. The square planar crystal-field splitting is also crucial in opening a robust insulating gap in Na$_4$IrO$_4$, irrespective of the specific magnetic ordering or treatment of electronic correlations. Spin-orbit coupling plays a minor role in shaping the electronic structure, but leads to strong magnetocrystalline anisotropy. The easy axis perpendicular to the IrO$_4$ plaquette, well explained using perturbation theory, is again closely related to the square planar coordination. Finally, the large single-ion anisotropy suppresses the spin frustration and stabilizes a collinear antiferromagnetic long-range magnetic ordering, as confirmed by Monte Carlo simulations predicting a quite low Néel temperature, expected from almost isolated IrO$_4$ square planar units that act as crystalline building blocks.

I. INTRODUCTION

Recently, $5d$ Ir oxides (iridates) have attracted extensive attention, due to the delicate competition between the on-site Coulomb correlation U, Hund's coupling J_H, spin-orbit coupling (SOC), and crystal-field splitting [1–4]. New phases, emerging phenomena, and fascinating physical properties have been uncovered in iridates. For example, Ir-based pyrochlores display a strong enhancement of SOC by correlations, changing from topological band insulator into topological Mott insulator [1], and orthorhombic perovskite iridates AIrO$_3$ ($A =$ alkaline-earth metal) are proposed as a new class of topological crystalline metals [4]. Most of these studies focused on tetravalent (Ir^{4+}, $5d^5$) iridates, sharing the IrO$_6$ octahedron as a common crystalline basis block, where the $5d$ states are split into triply degenerate t_{2g} states and doubly degenerate e_g states by the octahedral crystal field (see Fig. 1). As a result of the interplay between SOC and crystal-field splitting, the sixfold degenerate (including the spin degree of freedom) Ir t_{2g} states are split into completely filled quartet $J_{eff} = 3/2$ and half-filled doublet $J_{eff} = 1/2$ states [5,6]. The half-filled $J_{eff} = 1/2$ level with a hole state is proposed to be a key factor in driving exotic phenomena in iridates [3].

To the best of our knowledge, Ir atoms in iridates have been almost exclusively bonded to oxygen atoms in the form of octahedra. On the contrary, Na$_4$IrO$_4$ features one of the few examples of square planar coordination geometry in iridates (Fig. 1), composed by loosely connected IrO$_4$ square planar plaquettes [7,8]. Na$_4$IrO$_4$ was first synthesized by Mader and Hoppe [7], and recently revisited by Jansen and co-workers [8]. The isolated square planar IrO$_4$ plaquettes locate in the ab plane with tiny deviations of the Ir-O bonds from the crystallographic a/b axis. For each Ir atom, there

are two nearest-neighbor (NN) Ir atoms along the c axis and eight next-nearest-neighbor (NNN) Ir atoms along the lattice diagonal. Na$_4$IrO$_4$ can therefore be viewed as consisting of rigid IrO$_4$ clusters almost separated one from the other, arranged on a body-centered tetragonal lattice. The most remarkable feature in Na$_4$IrO$_4$ is therefore the uncommon local geometry of the IrO$_4$ plaquette, which will lead the d orbitals to further split under a square planar crystal field (as schematically shown in Fig. 1) [8]. The square planar geometry is frequently found in $3d$ transition-metal compounds, such as the T' structural electron-doped cuprate superconductors [9], and the infinite-layer cuprates SrCuO$_2$ and CaCuO$_2$ or iron oxide SrFeO$_2$ [10]. However, square planar units are corner sharing in these $3d$ compounds, whereas IrO$_4$ square planar units are separated one from the other in Na$_4$IrO$_4$ (see Fig. 1). The crystalline building blocks of IrO$_4$ plaquettes resemble the isolated CuO$_4$ plaquettes in the quasi-zero-dimensional compound CuB$_2$O$_4$, displaying very complex magnetic phases and remarkably strong magneto-optical effects [11–13]. One of the few experimental investigations on Na$_4$IrO$_4$ revealed a temperature dependence of the magnetic susceptibility exhibiting clear antiferromagnetic (AFM) ordering at 25 K [8], although the detailed magnetic structure was not reported. First-principles density functional theory (DFT) calculations proposed the crucial role of effective Coulomb interactions (Hubbard U) in determining the crystal structure of Na$_4$IrO$_4$. In contrast, the magnetic ordering and SOC was reported to play almost no role in the crystal-field splitting, orbital filling, and structural instability of Na$_4$IrO$_4$ [8].

In the present work, we explored the electronic structure, magnetocrystalline anisotropy (MCA), and spin-exchange interactions in Na$_4$IrO$_4$ by performing DFT calculations, complemented by Monte Carlo (MC) simulations to predict the phase transition temperature and magnetic ground state. All the remarkable properties of Na$_4$IrO$_4$ are closely related to the crucial square planar coordination in IrO$_4$ plaquettes. The
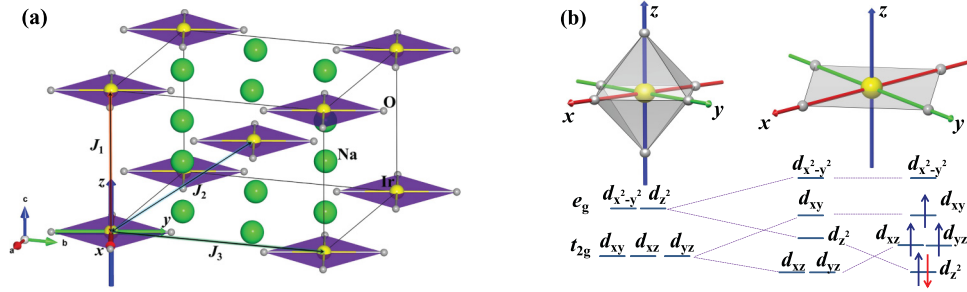
*silvia.picozzi@spin.cnr.it

FIG. 1. (a) Crystal structure and spin-exchange paths (J_1, J_2, and J_3) of Na_4IrO_4. The large (green), middle (yellow), and small (gray) spheres represent the Na, Ir, and O ions, respectively. We use *xyz* for the local coordinates and *abc* for the global orientation. (b) Schematic *d*-orbital splittings under octahedral (left) and square planar (middle) crystal field, and the actual (right) orders of the energy level arrangements and the intermediate-spin state for Ir^{4+} ($5d^5$) ions in Na_4IrO_4 (see Sec. III A).

electronic structure shows an energy level splitting consistent with square planar crystal field and with strong hybridizations (both interatomic between Ir $5d$ and O $2p$ states as well as intra-atomic between Ir $5d_{z^2}$ and Ir $6s$ states), leading to an intermediate-spin state, quite unusual for iridates but expected from almost isolated square planar IrO_4 units. The insulating band gap originates from the strong crystal-field splitting, independently on the magnetic ordering and Coulomb interactions. SOC interactions almost have no effect on the electronic structure, but result in a large easy-axis MCA [single-ion anisotropy (SIA)] of the Ir^{4+} ion in the unusual square planar crystal field. Finally, our MC simulations predict a rather low Néel temperature and a collinear long-range AFM magnetic ordering in Na_4IrO_4, again expected from loosely connected square planar IrO_4 plaquettes.

The present paper is organized in the following way. In Sec. II, we describe the calculation methods and the crystal structure of Na_4IrO_4. The electronic structure details, MCA, magnetic properties, and spin-exchange interactions are described and discussed in Sec. III. The results are summarized in Sec. IV.

II. COMPUTATIONAL METHODS AND STRUCTURAL DETAILS

Electronic structure calculations were carried out using the Vienna *Ab Initio* Simulation Package (VASP) code [14] within the projector augmented wave (PAW) method [15,16].

The generalized gradient approximation (GGA) exchange-correlation functional as parametrized by the Perdew-Burke-Ernzerhof (PBE) was used for all spin-polarized calculations [17]. SOC was included in the simulations using the non-collinear magnetism settings. The rotationally invariant $+U$ method introduced by Liechtenstein *et al.* was employed to account for correlation effects [18]. The values of the Coulomb interactions U and the Hund's coupling J_H for Ir $5d$ orbitals were fixed to 2 and 0.2 eV, respectively. K-point meshes of $8 \times 8 \times 12$ for the primitive unit cell and $6 \times 6 \times 6$ for $\sqrt{2} \times \sqrt{2} \times 2$ supercell (see below) were used for the Brillouin zone integration. The cutoff energy was set to 520 eV for all DFT calculations. The threshold for self-consistent-field energy convergence was chosen as 10^{-6} eV.

X-ray crystal structure refinements of Na_4IrO_4 show a tetragonal structure (space group $I4/m$) with two formula units (f.u.) per unit cell [7,8]. According to the symmetry, Na, Ir, and O atoms can be classified as three nonequivalent crystallographic sites in the unit cell. They are located at $8c$ (x, y, 0), $2a$ (0, 0, 0), and $8h$ (x, y, 0) sites, respectively. From x-ray diffraction experiments, the lattice constants of Na_4IrO_4 were determined to be $a = b = 7.184$ Å and $c = 4.725$ Å [8]. In the IrO_4 square plane, the two O-Ir-O bonds are mutually perpendicular but slightly deviating from the global crystallographic a/b axis in the ab plane. To monitor the behavior of the square planar crystal field, a local coordinate system (x, y, z) defined in Fig. 1 is employed for Ir atoms, with z being exactly perpendicular to the IrO_4 square plane,
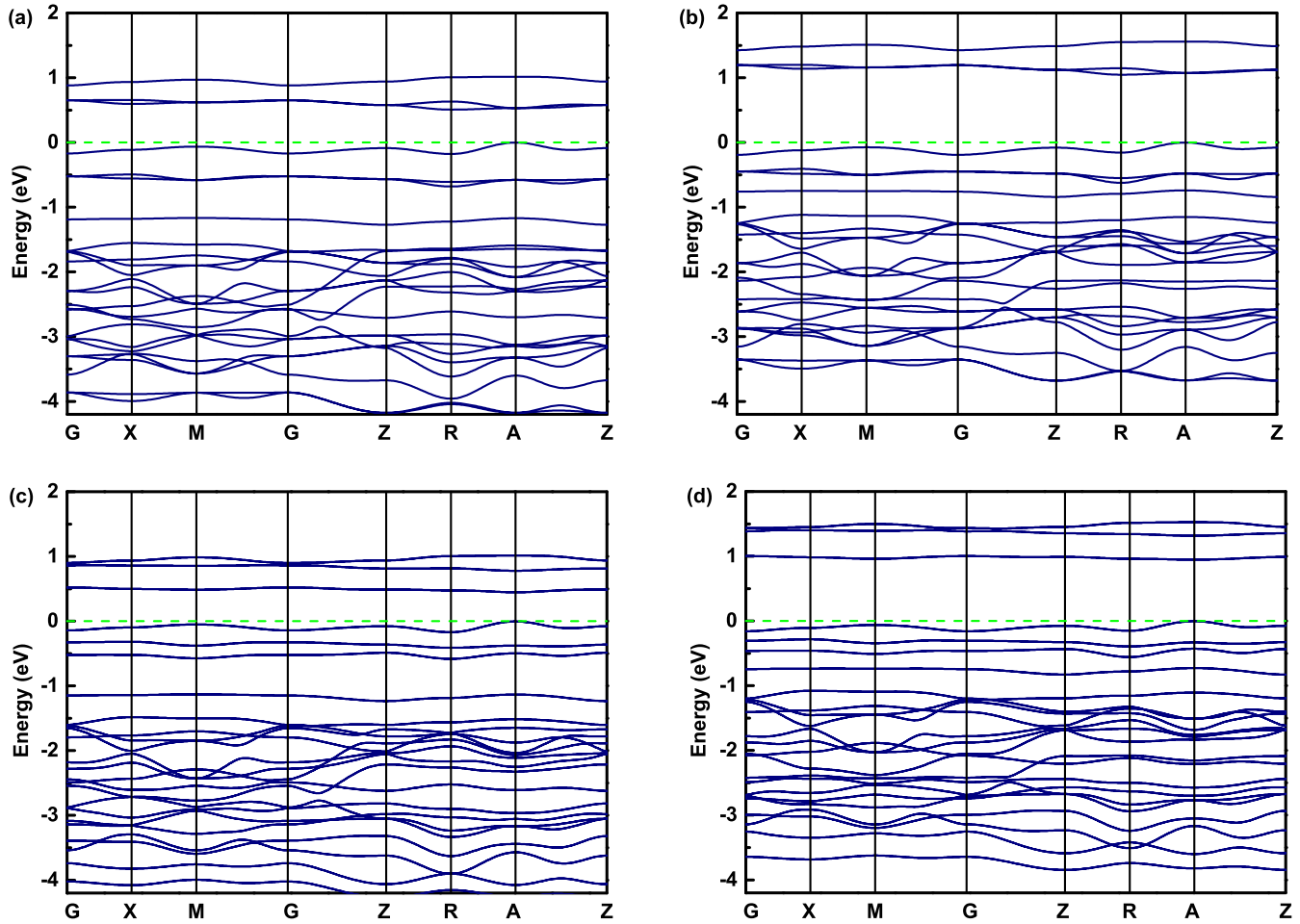
TABLE I. Theoretical calculated and experimental measured lattice constants (Å), unit cell volume (V, Å^3), atomic internal coordinates, and Ir-O bond length (Å) of Na_4IrO_4.

				Na		O		
	$a = b$	c	V	x	y	x	y	Ir-O
Expt.[a]	7.167	4.713	242.09	0.1962	0.4059	0.2526	0.0815	1.902
Expt.[b]	7.184	4.725	243.85					1.942
Theor.[b]	7.207	4.704	244.33					1.938
GGA[c]	7.256	4.759	250.53	0.1974	0.4049	0.2538	0.0826	1.937
GGA + U[c]	7.280	4.742	251.33	0.1966	0.4028	0.2525	0.0819	1.932
GGA+SOC[c]	7.262	4.755	250.78	0.1972	0.4043	0.2536	0.0824	1.937
GGA + SOC + U[c]	7.287	4.739	251.63	0.1965	0.4024	0.2524	0.0818	1.933

[a]Reference [7].
[b]Reference [8].
[c]Present work.

FIG. 2. Band structure of Na$_4$IrO$_4$ calculated within (a) GGA, (b) GGA $+ U$, (c) GGA+SOC, and (d) GGA $+$ SOC $+ U$, where $U = 2$ eV. Since spin-up and spin-down states are degenerate in the AFM state, only spin-up subbands are reported in (a,b).

and x, y are defined exactly along one of the Ir-O bonds in the square planar IrO$_4$ plaquette.

Based on experimental lattice parameters, we optimized all independent atomic internal coordinates and lattice constants. As the detailed magnetic structure is not available [8], the AFM ordering has been simulated by considering an antiparallel alignment of the spin magnetic moment of two Ir atoms in the unit cell, found from first principles to be the lowest-energy magnetic ground state (see Sec. III C). We confirmed that a reasonable U parameter and SOC have only a small impact on the crystal structure. As listed in Table I, our theoretical calculated lattice parameters were in good agreement with available experimental and theoretical results, with errors less than 2% for the lattice constants and 4% for the volume. We noted that smaller errors and results similar to Ref. [8] can be obtained for a nonmagnetic state setting. Electronic structure calculations were carried out with the relaxed lattice parameters for the AFM state. First, we performed spin-polarized calculations within GGA, and then took Coulomb interactions U and SOC into account by GGA $+ U$, GGA+SOC, and GGA $+$ SOC $+ U$ calculations. For the SOC calculations, the quantization axis was set along [0 0 1] (the crystallographic c axis, except where specifically noted otherwise).

III. RESULTS AND DISCUSSIONS

A. Electronic structure and local magnetic moments

As shown in Fig. 2, the band structures show strong localized and flat-band character around the Fermi level (E_F), indicating weak interactions because of the loosely connected crystal structure [Fig. 1(a)]. Unlike other iridates, an insulating gap has opened up even without Coulomb interaction corrections for the AFM state [Fig. 2(a)]. Upon inclusion of Coulomb interactions, the band gap remarkably increases, although the essential characteristics of the band dispersion are unaffected [Fig. 2(b)]. Furthermore, as presented in Figs. 2(c) and 2(d), except for lifting the degeneracy of the $d_{xz,yz}$ bands [8], the main features of the band structures remain unchanged with or without SOC. As shown in Ref. [8], an insulating energy gap was obtained even assuming ferromagnetic (FM) ordering, so that the insulating nature in Na$_4$IrO$_4$ does not depend on the magnetic ordering state, Coulomb parameters, and SOC, rather being essentially determined by the crystal-field splitting of the unusual IrO$_4$ square planar units.

The detailed electronic structure can be further inspected by the projected density of states (pDOS). As shown in Fig. 3, due to the interatomic interactions between the central Ir and
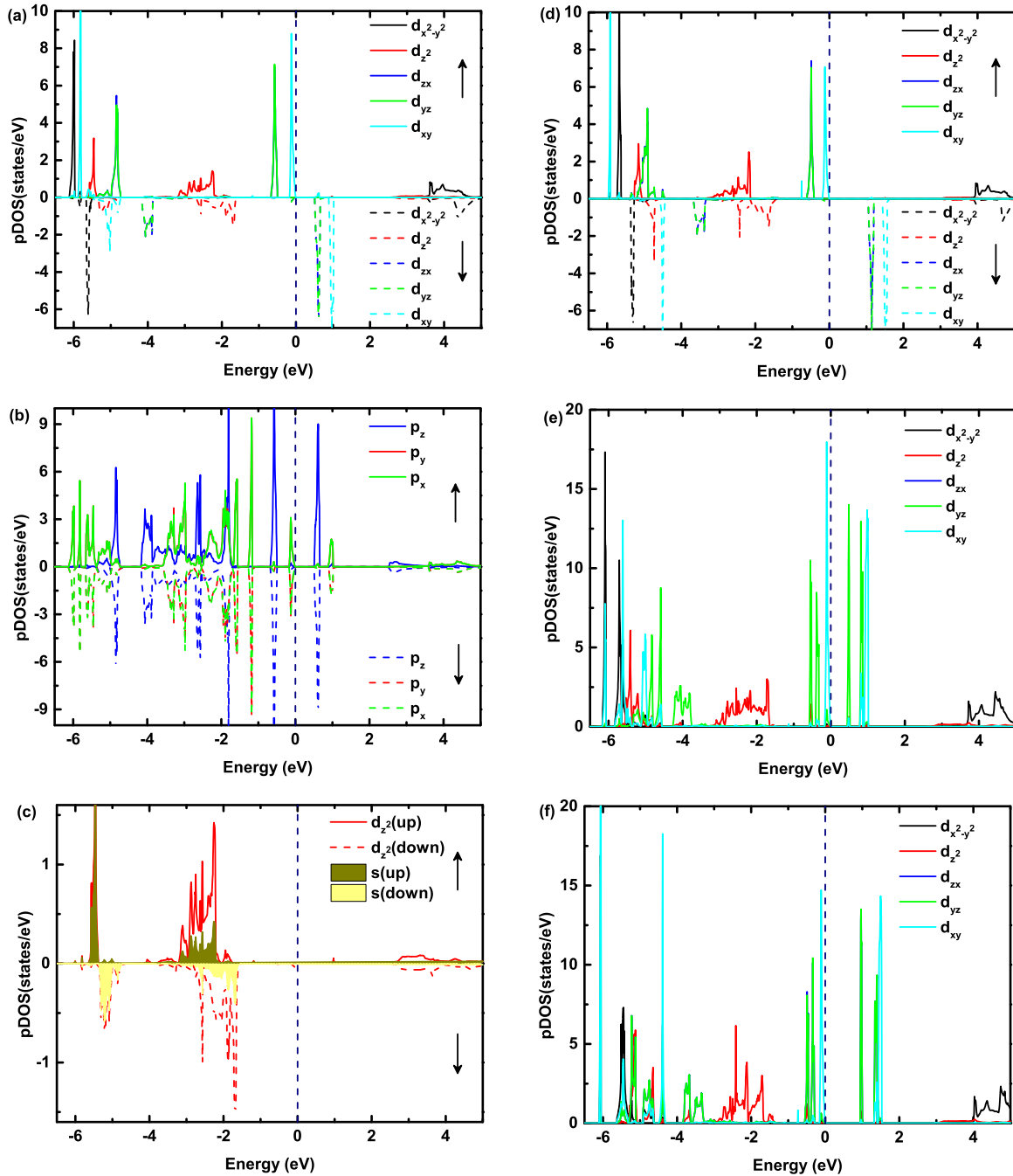
FIG. 3. Projected density of states (pDOS): (a) Ir $5d$, (b) O $2p$, and (c) Ir intra-atomic $5d_{z^2}$ and $6s$ states calculated within GGA; (d–f) show Ir $5d$ states calculated within GGA $+ U$, GGA+SOC, and GGA $+$ SOC $+ U$, respectively. Due to the structural symmetry, the Ir $5d_{yz}$ and d_{xz} states overlap.

four ligand oxygen ions, the Ir^{4+} $5d$ states form bonding (ranging from -6 to -4 eV) and antibonding (from -3 to 1 eV) molecular orbitals, with the Ir antibonding states located around E_F and distinctly split off. This situation is well consistent with the typical energy level splitting of d orbitals under a square planar crystal field [19], which is so strong that Ir^{4+} ($5d^5$) adopts an intermediate-spin state [see Fig. 1(b)]. O $2p$ bands are mainly located in a lower energy range, although the pDOS shows a strong interatomic hybridization between Ir $5d$ and O $2p$ states. An insulating gap opens up between different spin channels of spin-up (spin-down) d_{xy} and

spin-down (spin-up) $d_{xz,yz}$ orbitals due to the large exchange splitting. The Ir d_{z^2} orbitals are the lowest-lying occupied states for both spin channels. The double occupation of the d_{z^2} orbital [rather than the degenerate $d_{xz,\,yz}$ orbitals; see Figs. 1(b) and 4(d)], seemingly at variance with the expectation from crystal-field theory for the D_{4h} point symmetry [see the conventional energy level sequence schematically shown in Fig. 1(b), bottom middle] [10], also occurred in another infinite-layer $3d$ oxide, SrFeO$_2$, with perfect square planar coordination [10,19,20]. The origin of the d_{z^2}-double occupation arises from the reduction of Coulomb repulsion interactions, due to the
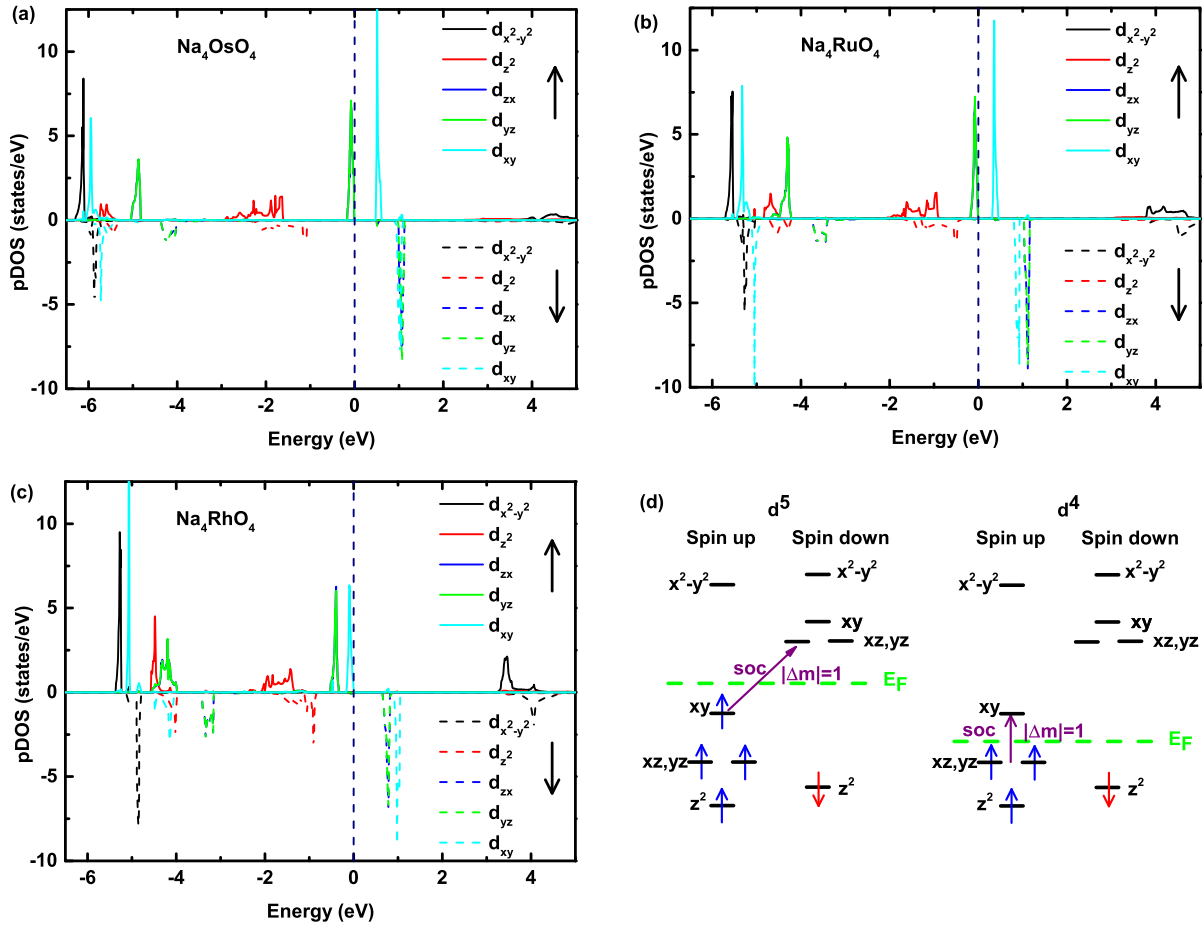
FIG. 4. The pDOS of M d states for Na_4MO_4 compounds (M = Os^{4+}, Ru^{4+}, and Rh^{4+}): (a) Os $5d$, (b) Ru $4d$, and (c) Rh $4d$ states calculated within GGA. Panel (d) shows the schematic energy level splitting by the square planar crystal field and the orbital occupations for the d^5 and d^4 configuration, where the SOC between unperturbed occupied and unoccupied d states is explicitly highlighted.

missing oxygen atoms in the direction perpendicular to the IrO_4 square plane (see Fig. 1) [21]. In addition, according to the D_{4h} point group symmetry, the Ir $5d_{z^2}$ and $6s$ orbitals have the same a_{1g} symmetry, therefore resulting in their intra-atomic hybridization [see pDOS in Fig. 3(c)] and, in turn, in a large reduction of the exchange splitting for the d_{z^2} orbitals and, finally, in their double occupation [22].

SOC often significantly influences the $5d$ band dispersion and plays an essential role in the insulating ground state for many iridates, with the formation of the half-filled $J_{eff} = 1/2$ spin-orbit insulating states [5,6,23,24]. The Ir^{4+} ions in these iridates all show low-spin $5d^5$ (t_{2g}^5, e_g^0) electronic configurations. However, as demonstrated in Fig. 2, the difference between the band structures with and without SOC is small in Na_4IrO_4. In addition, different coordination environments (square planar vs octahedral) and related crystal fields result in distinct energy level splitting and orbital occupation patterns. As presented in Fig. 3, just considering the antibonding states, the d-electron configuration in Na_4IrO_4 organizes as $(z^2)^1 < (xz,yz)^2 < (xy)^1 < (x^2-y^2)^0$ for the spin-up states, and in sequence $(z^2)^1 < (xz,yz)^0 < (xy)^0 < (x^2-y^2)^0$ for the spin-down states [schematically shown in Fig. 1(b)]. Due to the strong crystal-field splitting, the lowest d_{z^2} states and the highest $d_{x^2-y^2}$ states are located far from the other three, d_{xy}, d_{yz}, and d_{zx}, states (generally defined as t_{2g} orbitals

in octahedral or tetragonal crystal field). In this sense, the electronic configurations of intermediate-spin state Ir^{4+} ions in Na_4IrO_4 can be viewed as reduced to a d^3 (t_{2g}^3, $S = 3/2$) system and the orbital degree of freedom can be thought as being quenched ($L_{eff} = 0$) for a half-filled t_{2g} band, in which case SOC enters only as a third-order perturbation [25]. According to the SOC Hamiltonian $\hat{H}_{SO} = \lambda \hat{S} \cdot \hat{L}$, this could justify why SOC does not play a dominant role in the electronic structure [26–28].

In contrast with other $5d^5$ iridates [5,29], as shown in Table II, the orbital moment of Ir^{4+} ions is much smaller than the spin moment in Na_4IrO_4, indicating that the orbital degree

TABLE II. Calculated spin moment (M_S) and orbital moment (M_L) of Na_4IrO_4 (values in Bohr magnetons, positive/negative signs indicate the moment directions).

| | M_S | | M_L | |
	Ir	O	Ir	O
GGA	±1.585	±0.248		
GGA + U	±1.744	±0.24		
GGA+SOC	±1.424	±0.229	∓0.071	±0.017
GGA + SOC + U	±1.592	±0.224	∓0.045	±0.019

of freedom is indeed almost quenched and the SOC effect is small. In addition, the orbital moments are antiparallel to the spin moments for Ir^{4+} ions, whereas the orbital moments are parallel to the spin moments for O^{2-} ions. These results follow Hund's third rule, according to which the orbital moment and spin moment should be antiparallel (parallel) for a less (more) than half-filled system. Although the calculated spin moment of Ir^{4+} ions is smaller than $3\,\mu_B$ for a nominal $S = 3/2$ intermediate-spin $5d^5$-electron system, the spin moment contributions from O atoms are notably large, revealing strong interatomic hybridizations of Ir $5d$ and O $2p$ states, consistent with the pDOS (see Fig. 3). A reduced value of spin moment is very common in iridates because of the strong interatomic hybridizations between Ir $5d$ and O $2p$ states [5,29–35]. However, the spin moments are often smaller than $0.5\,\mu_B$ for Ir^{4+} ions in other octahedral-coordinated iridates [5,29,31–35], whereas the hybridization-driven reduction is far smaller in Na_4IrO_4, resulting in large local magnetic moments. At the same time, the orbital moments are often as large as twice the spin moment in other iridates, where the strong SOC and the large octahedral crystal-field splitting produce an effective $J_{eff} = 1/2$ state for the Ir^{4+} ion [5]. The Coulomb interactions are often one order of magnitude smaller in iridates with respect to $3d$-based oxides, and the $5d$ transition-metal oxides are expected to be more itinerant because of the larger spatial extent of $5d$ orbitals [35]. However, the effective electronic correlations increase upon decreasing connectivity of IrO_6 octahedra in iridates [36]. Therefore, due to the peculiar crystal structure and square planar crystal-field splitting, at variance with the expectation from the itinerancy of $5d$ iridates, Na_4IrO_4 is the only iridate showing an intermediate-spin state with large local spin moments, as demonstrated by the localized flat-band structure and isolated energy levels of Na_4IrO_4 (Fig. 2).

B. MCA and preferred spin orientations

In this section we focus on the MCA in Na_4IrO_4 and, for clearer insights, compare it with MCA in other hypothetical $4d$ and $5d$ compounds with square planar crystal field. Using the initial crystal structure of Na_4IrO_4, we replace the Ir ions by Ru^{4+} ($4d^4$), Rh^{4+} ($4d^5$), and Os^{4+} ($5d^4$) ions, respectively. For these hypothetical Na_4MO_4 compounds ($M =$ Ru, Rh, and Os), when all the independent atomic internal coordinates and Bravais lattices are allowed to fully relax (including possible relaxation to different space group, coordination, etc.), the lattice symmetry of Na_4IrO_4 and the related square planar coordination are kept as ground state (in contrast to what happens for $3d$-based Na_4CoO_4, where the oxygen cage around the $3d$ metal turns to tetrahedral [8]). Our calculations predict these Na_4MO_4 compounds to show optimized lattice parameters very similar to Na_4IrO_4. As reported in Table III, the total energy within GGA+SOC (with or without U) strongly depends upon the relative orientation of the spin quantization axis, leading to a sizable MCA. While this is consistent with the strongly anisotropic coordination in IrO_4 "isolated" plaquettes, it would be interesting to experimentally investigate this aspect.

In particular (see Table III), for Na_4IrO_4 and Na_4RhO_4 with d^5 electronic configurations, the configuration with the spin moments parallel to the c axis (out of plane) is more stable

TABLE III. Calculated MCA energy per M atom (meV) for Na_4MO_4 ($M =$ Ru, Rh, Os, and Ir). Total energy values for the spin quantization axis (SAXIS) in the ab plane (local [100] and [110] direction) are given with respect to the energy for the SAXIS out of plane (local [001] direction), taken as reference. The SIA energies (meV) for Na_4IrO_4 with one Ir atom and three nonmagnetic Si ions are given in parentheses.

	SAXIS	Ru	Rh	Os	Ir
GGA+SOC	[001]	0	0	0	0
	[100]	–4.87	1.80	–21.09	14.88(14.03)
	[110]	–4.86	1.78	–21.43	12.97(12.09)
GGA + SOC + U	[001]	0	0	0	0
	[100]	–4.34	1.65	–13.17	15.99(15.74)
	[110]	–4.36	1.63	–13.86	14.69(14.44)

than that with the spin moments in the ab plane. In contrast, for Na_4OsO_4 and Na_4RuO_4 with d^4 electronic configurations, the states with the spin moments in the ab plane are energetically favored. In other words, the d^5 compounds show an easy-axis anisotropy, whereas the d^4 compounds show an easy-plane anisotropy.

The MCA and preferred spin orientations can be analyzed via perturbation theory [37–40], where SOC is included to couple spin and orbital angular momentum ($\hat{S}$ and $\hat{L}$), resulting in the SOC Hamiltonian, $\hat{H}_{SO} = \lambda \hat{S} \cdot \hat{L}$, λ being the SOC constant. Employing two independent coordinate systems (x, y, z) and (x', y', z') for the orbital $\hat{L}$ and spin $\hat{S}$, respectively, the SOC Hamiltonian $\hat{H}_{SO} = \lambda \hat{S} \cdot \hat{L}$ is rewritten as $\hat{H}_{SO} = \hat{H}_{SO}^0 + \hat{H}_{SO}'$, where the "spin-conserving" term

$$\hat{H}_{SO}^0 = \lambda \hat{S}_{z'} \left(\hat{L}_z \cos\theta + \tfrac{1}{2}\hat{L}_+ e^{-i\phi} \sin\theta + \tfrac{1}{2}\hat{L}_- e^{+i\phi} \sin\theta \right)$$
$$= \lambda \hat{S}_{z'} \left(\hat{L}_z \cos\theta + \hat{L}_x \sin\theta \cos\phi + \hat{L}_y \sin\theta \sin\phi \right),$$
$$(1)$$

and the "spin-nonconserving" term

$$\hat{H}_{SO}' = \frac{1}{2}\lambda \hat{S}_{+'} \left(-\hat{L}_z \sin\theta - \hat{L}_+ e^{-i\phi} \sin^2\frac{\theta}{2} + \hat{L}_- e^{+i\phi} \cos^2\frac{\theta}{2} \right)$$
$$+ \frac{1}{2}\lambda \hat{S}_{-'} \left(-\hat{L}_z \sin\theta + \hat{L}_+ e^{-i\phi} \cos^2\frac{\theta}{2} - \hat{L}_- e^{+i\phi} \sin^2\frac{\theta}{2} \right)$$
$$= \frac{1}{2}\lambda (\hat{S}_{+'} + \hat{S}_{-'})(-\hat{L}_z \sin\theta$$
$$+ \hat{L}_x \cos\theta \cos\phi + \hat{L}_y \cos\theta \sin\phi),$$
$$(2)$$

where θ and ϕ define the magnetization direction (z') with respect to the (x, y, z) coordinate system (for the coordinate system, the reader can also refer to Scheme 22 in Ref. [38] or Fig. 2 in Ref. [40]). The energy correction by SOC is given by

$$\Delta E_{soc} = \sum_{e,g} \frac{|\langle g|\hat{H}_{soc}|e\rangle|^2}{E_g - E_e},$$
$$(3)$$

where $|g\rangle$ and $|e\rangle$ are the ground (occupied) and excited (unoccupied) states; E_g and E_e are the corresponding unperturbed energies [37–42].

The pDOS in Figs. 3 and 4 indicate that the crystal-field splitting is the same for these isostructural $4d$ and $5d$ compounds and are typical of square planar splitting [10,19–22]. The crystal-field splitting is so strong that Ru^{4+} ($4d^4$), Rh^{4+} ($4d^5$), Os^{4+} ($5d^4$), and Ir^{4+} ($5d^5$) ions all adopt intermediate-spin states with double occupation of the d_{z^2} orbitals. Due to the large spin-exchange splitting and crystal-field splitting, even without Hubbard U corrections, the insulating gaps open up between different (the same) spin channels for Na_4IrO_4 and Na_4RhO_4 (Na_4OsO_4 and Na_4RuO_4) with d^5 (d^4) electronic configurations.

With the same d^5 electronic configurations, Na_4IrO_4 and Na_4RhO_4 display identical energy level splitting and orbital occupations (as shown in the pDOS of Figs. 3 and 4), where the smallest energy gap between the occupied and unoccupied levels occurs between the d_{xy} (spin-up) and the $d_{xz,\,yz}$ (spin-down) levels. As displayed in Fig. 4(d), these levels differ in their magnetic orbital quantum number $|\Delta m|$ by 1 [38,39]. Because the occupied and unoccupied d states couple within opposite-spin channels, the SOC Hamiltonian will be governed by spin-nonconserving term $\hat{H}'_{SO}$ [Eq. (2)], and the perturbation matrix element $\langle g|\hat{H}_{soc}|e\rangle$ will be proportional to $\cos\theta$ [43]. As such, the SOC-induced interactions are maximized when the spin magnetization direction is parallel to the orbital z axis (i.e., $\theta = 0°$) in Na_4IrO_4 and Na_4RhO_4.

On the other hand, the situation is different when considering Na_4OsO_4 and Na_4RuO_4 with d^4 electronic configurations. As shown in the pDOS of Fig. 4, the d-electron configurations in Na_4OsO_4 and Na_4RuO_4 align as $(z^2)^1 < (xz,yz)^2 < (xy)^0 < (x^2-y^2)^0$ for the spin-up states, and in the order of $(z^2)^1 < (xz,yz)^0 < (xy)^0 < (x^2-y^2)^0$ for the spin-down states. As presented in the schematic energy diagram of Fig. 4(d), the smallest energy gap between the occupied and unoccupied levels occurs now in the same spin-up (or spin-down) channel for $d_{xz,\,yz}$ and d_{xy} orbitals, differing in their magnetic orbital quantum number $|\Delta m|$ by 1 [38,39]. SOC interactions couple occupied and unoccupied d states within the same spin channel, so the SOC Hamiltonian will be governed by spin-conserving term $\hat{H}_{SO}$ [Eq. (1)], and the perturbation matrix element $\langle g|\hat{H}_{soc}|e\rangle$ will be proportional to $\sin\theta$ [43]. In this case, the SOC-induced interactions are maximized when the spin magnetization direction is perpendicular to the orbital z axis (i.e., $\theta = 90°$). Therefore, Na_4OsO_4 and Na_4RuO_4 show easy-plane anisotropy, in contrast with the easy-axis anisotropy in Na_4IrO_4 and Na_4RhO_4.

According to previous works [41,42], we can further evaluate the perturbation matrix element $\langle g|\hat{H}_{soc}|e\rangle$ and hence the energy correction by SOC. Noting that $\langle xy\uparrow|\hat{H}_{soc}|xy\downarrow\rangle = 0$, for the case of Na_4IrO_4 and Na_4RhO_4 with d^5 electronic configurations, the second-order energy shift is given by

$$\Delta E_{soc} = -\lambda^2 \left(\frac{1}{2\Delta_1} + \frac{1}{2\Delta_3} \right)$$
$$+ \lambda^2 \left(\frac{1}{4\Delta_1} - \frac{1}{2\Delta_2} + \frac{1}{4\Delta_3} \right) \sin^2\theta, \quad (4)$$

where Δ_1, Δ_2, and Δ_3 are the energy gaps for the occupied and unoccupied levels between the d_{xy} (spin-up) with $d_{xz,\,yz}$ (spin-down), $d_{xz,\,yz}$ (spin-up) with $d_{xz,\,yz}$ (spin-down), and $d_{xz,\,yz}$ (spin-up) with d_{xy} (spin-down) orbitals, respectively.

For the case of Na_4OsO_4 and Na_4RuO_4 with d^4 electronic configurations, the second-order energy shift is given by

$$\Delta E_{soc} = -\frac{\lambda^2}{2\Delta_1} + \lambda^2 \left(-\frac{1}{4\Delta_1} - \frac{1}{2\Delta_2} + \frac{1}{4\Delta_3} \right) \sin^2\theta, \quad (5)$$

where Δ_1, Δ_2, and Δ_3 are the energy gaps for the occupied and unoccupied levels between the $d_{xz,\,yz}$ (spin-up) with d_{xy} (spin-up), $d_{xz,\,yz}$ (spin-up) with $d_{xz,\,yz}$ (spin-down), and $d_{xz,\,yz}$ (spin-up) with d_{xy} (spin-down) orbitals, respectively.

As shown in Eqs. (4) and (5), the azimuthal ϕ dependence vanished in the perturbation theory up to second order for the energy shift. According to the energy level arrangements and the related energy gaps from the pDOS of Figs. 3 and 4, the angle-dependent parts of Eqs. (4) and (5) show a $\sin^2\theta$ dependence with positive (negative) values for the Na_4MO_4 compounds with d^5 (d^4) electronic configurations, indicating that the magnetization easy axis is out of (resides in) the ab plane. We recall that the simple dependence of the total energy on the magnetization angle θ deduced from second-order perturbation theory [41,44], can be expressed as

$$E(\theta) - E_0 = K_1 \sin^2\theta. \quad (6)$$

To carefully evaluate the dependence of total energy on θ, we performed a series of calculations by rotating the magnetization angle θ. As shown in Fig. 5, the calculated results fit well with what was expected from Eq. (6) for all the Na_4MO_4 (M = Ir^{4+}, Os^{4+}, Ru^{4+}, and Rh^{4+}) compounds. The MCA energy (MAE) curves display the opposite trend for the d^5 (Na_4IrO_4 and Na_4RhO_4) and d^4 (Na_4OsO_4 and Na_4RuO_4) compounds, consistently with the opposite sign of Eqs. (4) and (5) for the angle-dependent parts of the energy corrections by SOC. The MAE behavior [Fig. 5(a)] shows a minimum for Na_4IrO_4 and Na_4RhO_4 at the magnetization direction along the crystallographic c axis, corresponding to the easy-axis anisotropy (i.e., the $\theta = 0°$ spin orientation) of d^5 materials. In contrast, the MAE behavior [Fig. 5(b)] displays a minimum for Na_4OsO_4 and Na_4RuO_4 for magnetization perpendicular to the c axis, in line with the easy-plane anisotropy (i.e., the $\theta = 90°$ spin orientation) of d^4 materials.

C. Single-ion anisotropy and spin-exchange interactions

From a general point of view, SOC can lead to inter-site Dzyaloshinskii-Moriya (DM) (antisymmetric) interaction, anisotropic exchange, and single-ion (or single-site) anisotropy (SIA). According to the crystal symmetry, the DM interaction should not appear, due to the presence of inversion symmetry in Na_4IrO_4; as for anisotropic exchange, we expect it to be a small relativistic correction to the isotropic exchange. On the other hand, we focus on the SIA, which is mainly determined by the metal center and its first coordination crystal field [45]. As a further confirmation of the magnitude of the SIA for a specified Ir ion, we replaced the three neighboring Ir^{4+} ions with nonmagnetic Si^{4+} ions in a supercell doubled along the crystallographic c axis. In this way, all other intersite NN or NNN magnetic exchange interactions vanish and the
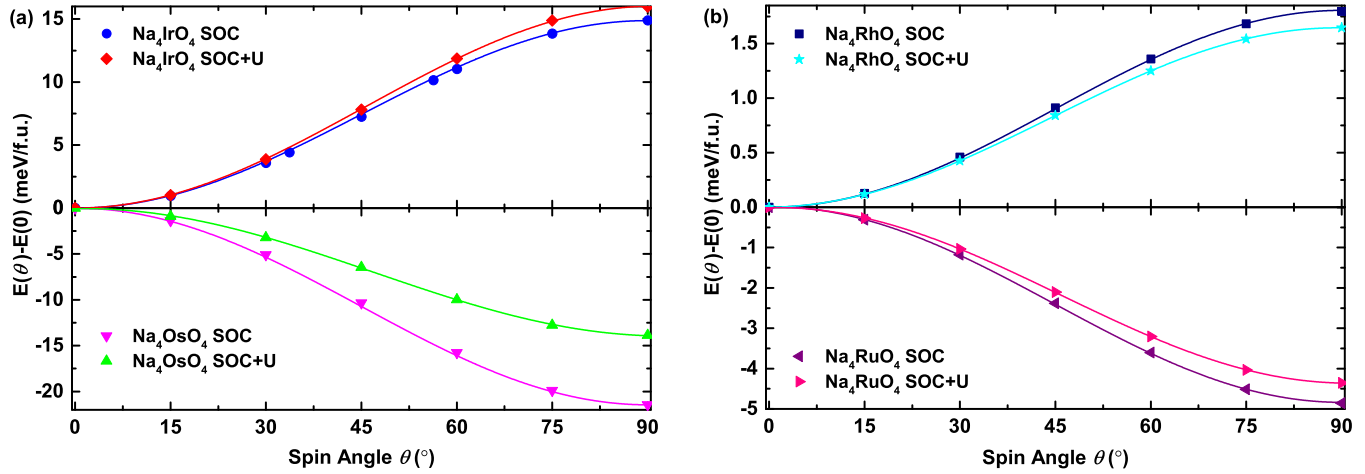
FIG. 5. Dependence of the total energy on the magnetization angle θ for the Na_4MO_4 ($M = Ir^{4+}$, Os^{4+}, Ru^{4+}, and Rh^{4+}) compounds and fitted with a function, like $A\sin^2\theta$ (the line). The calculations were performed within GGA including SOC (with or without U).

only contribution left is the SIA of the Ir^{4+} ion. After checking that the crystal-field splitting is unchanged with respect to the original configuration in Na_4IrO_4, our results (see Table III) show, as expected, a comparable magnitude of MCA and SIA energies.

In this context the title Na_4IrO_4 material presents a particularly intriguing puzzle, because SOC does have a minor influence on the band structure (Fig. 2) and the orbital moments are almost quenched [the electronic configurations of Ir^{4+} ions behave similar to the d^3 (t_{2g}^3, $S = 3/2$) system]; however, the low symmetry of the square planar local environment together with the SOC-induced SIA give rise to a giant magnetocrystalline anisotropy. As pointed out in Ref. [25] and references therein, the d^3 configurations are expected to be orbitally quenched states in octahedral coordination, yet there is clear experimental evidence that SOC influences the magnetic properties in $5d^3$ transition-metal oxides. An x-ray absorption near-edge spectroscopy plus x-ray circular dichroism study of $Ir^{6+}(5d^3)$ double perovskites Sr_2MIrO_6 found strong coupling between orbital and spin moments despite small orbital moments [46]; similar results were reported in the Os^{5+} ($5d^3$) materials Sr_2FeOsO_6 and Sr_2ScOsO_6 [47,48]. Furthermore, in another $5d$ compound, $NaOsO_3$, SOC also shows minor effects on the band structure, but leads to large magnetocrystalline energy differences in spite of orbital moments no greater than 0.1 μ_B [27,28]. We also note that even in $3d$ manganites, large magnetocrystalline anisotropy is observed with quenched angular momentum [49].

Based on DFT electronic structure calculations for various spin-ordered magnetic insulating states, the spin-exchange parameters can be obtained by mapping the relative energies of the magnetic ordered states onto a Heisenberg or Ising Hamiltonian [50–52]. Generally, the spin Hamiltonian can be described by the classical Heisenberg model:

$$H = -\frac{1}{2}\sum_{i,j} J_{i,j} S_i \cdot S_j, \quad (7)$$

where S_i represents a spin operator at site i of the compound and the negative (positive) values of J denote AFM (FM) interactions, respectively.

The spin-exchange parameters J_1, J_2, and J_3 in Na_4IrO_4 are illustrated in Fig. 1. Based on the optimized lattice parameters for the AFM unit cell as shown in Table I within GGA, we artificially construct five special magnetic ordering states (i.e., FM, AFM1, AFM2, AFM3, and AFM4). The hypothetical FM state corresponds to a parallel alignment of all magnetic moments, whereas the other four AFM states are symmetry-broken arrangements in the $\sqrt{2} \times \sqrt{2} \times 2$ supercell (Fig. 6).

As shown by the DFT calculation results, the Ir^{4+} ions are in intermediate-spin states with formal $S = 3/2$ in Na_4IrO_4 [see Fig. 4(d)]. In terms of exchange parameters, the spin-exchange interaction energies (per f.u.) of the five magnetic ordering states are written as

$$E_{FM} = -\frac{9}{4}(J_1 + 4J_2 + 2J_3),$$
$$E_{AFM1} = -\frac{9}{4}(-J_1 - 2J_3),$$
$$E_{AFM2} = -\frac{9}{4}(J_1 - 4J_2 + 2J_3), \quad (8)$$
$$E_{AFM3} = -\frac{9}{4}(-J_1 + 2J_3),$$
$$E_{AFM4} = -\frac{9}{4}(J_1 - 2J_3).$$

Thus, by mapping the energy differences of these states in terms of the spin-exchange parameters with the corresponding energy differences from DFT calculations, we obtain

$$J_1 = -\frac{2}{9}(E_{AFM4} - E_{AFM1}),$$
$$J_2 = \frac{1}{18}(E_{AFM2} - E_{FM}), \quad (9)$$
$$J_3 = -\frac{1}{9}(E_{AFM3} - E_{AFM1}).$$

Using the calculated energy values of the five magnetic ordering states, we obtain the spin-exchange parameters summarized in Table IV. SOC has a small impact on the spin-exchange parameters, whereas the Coulomb interactions show remarkable influence, because the exchange coupling parameters J are inversely proportional to the Hubbard U [21]. The AFM2 state is the most stable, its total energy being lower than the other four magnetic states. The energies of the AFM1 state are comparable to the AFM3 state, reflecting very weak spin coupling interactions J_3 in the ab plane. The negligible J_3 is consistent with the loosely connected crystal structure
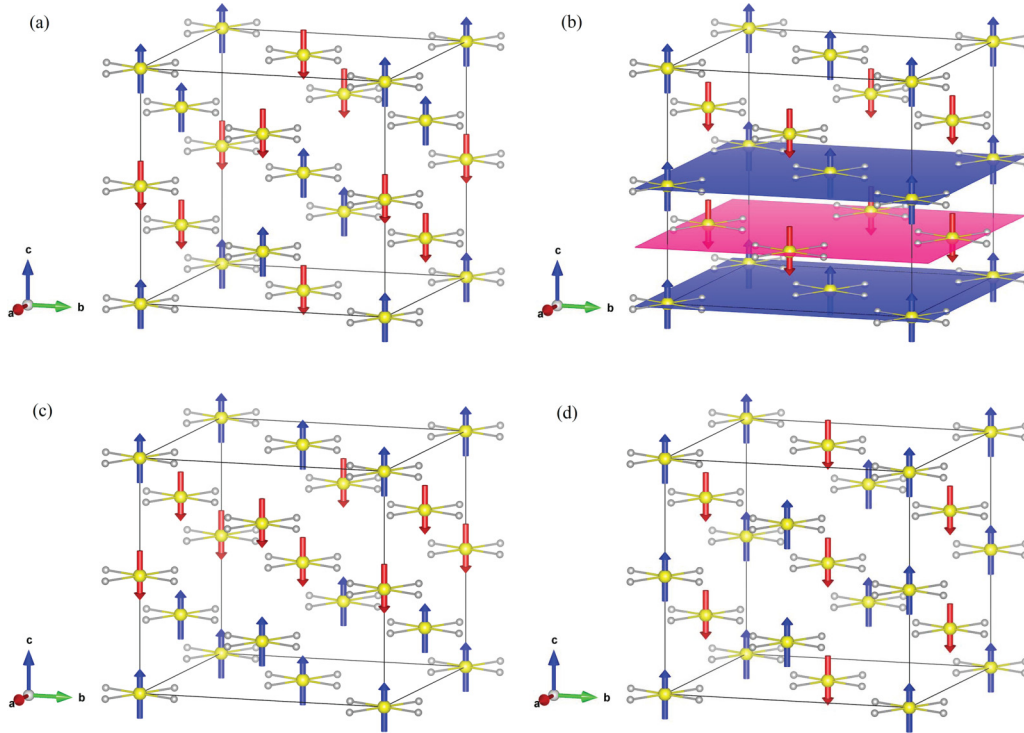
FIG. 6. Schematic representations of the four hypothetical AFM spin-ordering arrangements in the $\sqrt{2} \times \sqrt{2} \times 2$ supercell (only IrO$_4$ square plane are shown for clarity): (a) AFM1 (all magnetic moments are antiparallel to each other both in the ab plane and along the c axis), (b) AFM2 (all magnetic moments are parallel to each other both in the ab plane and along the c axis, but the NNN magnetic moments are antiparallel aligned), (c) AFM3 (all magnetic moments are antiparallel to each other along the c axis, but parallel aligned in the ab plane), and (d) AFM4 (all magnetic moments are parallel to each other along the c axis, but antiparallel aligned in the ab plane). The big (yellow) and small (gray) spheres denote the Ir and O atoms; the up (down) arrows represent the magnetic moment orientations. The FM planes for the AFM2 magnetic ground state are highlighted in (b), in order to better illustrate the stacking of FM planes antiferromagnetically coupled along the c axis.

and the large in-plane distances (about 7.2 Å) between the Ir^{4+} ions along the a or b axis. The other two spin-exchange interactions, J_1 and J_2, are AFM, and the NN interaction J_1 is smaller than the NNN interaction J_2, showing an inverse trend with respect to the distances for the NN (about 4.7 Å along the c axis) and NNN (about 5.6 Å along the diagonal of the unit cell) Ir^{4+} ions. However, this is reasonable, when considering the unusual crystal structure of Na$_4$IrO$_4$, where a given Ir site has two NN and eight NNN coordination Ir^{4+} ions. It should also be noted that both the NN and NNN interactions are AFM, so a geometrical magnetic frustration might arise in Na$_4$IrO$_4$, as the system cannot simultaneously satisfy all the NN and NNN AFM spin-exchange interactions. However the large SIA favors the collinear alignment of the magnetic moments. Indeed, according to the experimental results [8], the frustration index $f = |\theta|/T_N$ is close to 3, and the calculated ratios of J_1/J_2 are far from 1 in all the cases (see Table IV).

Therefore a spin frustration does not occur, as confirmed by the AFM ordering obtained from magnetic susceptibility measurements [8].

Using the UppASD (Uppsala Atomistic Spin Dynamics) package [53], we perform MC simulations to capture the dynamical properties of the spin systems at finite temperatures for a $16 \times 16 \times 16$ supercell based on the classical spin Hamiltonian [21]:

$$H = -\frac{1}{2} \sum_{i,j} J_{i,j} S_i \cdot S_j + \sum_i K S_{iz}^2, \qquad (10)$$

where the spin-exchange parameters $J_{i,j}$ within GGA $+$ SOC $+ U$ are summarized in Table IV, while the SIA energy $K S_{iz}^2$ is given in Table III. To obtain the transition temperature T_N, we evaluate the order parameter (i.e., staggered magnetization related to the AFM2 magnetic configuration) and the

TABLE IV. Energy difference relative to the reference AFM2 state (meV/f.u.) and calculated spin-exchange parameters (meV).

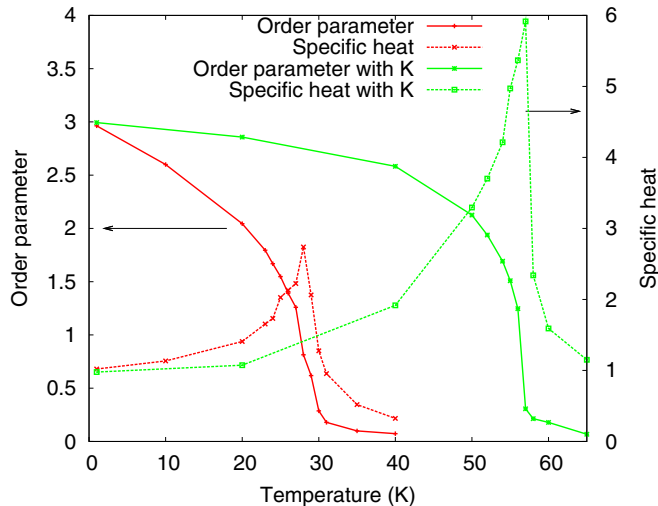|	AFM1	AFM2	AFM3	AFM4	FM	J_1	J_2	J_3	J_1/J_2
GGA	9.21	0	9.05	11.33	23.74	−0.47	−1.32	0.02	0.36
GGA $+ U$	4.21	0	4.09	6.16	12.61	−0.43	−0.70	0.01	0.62
GGA+SOC	8.48	0	8.27	10.50	21.93	−0.45	−1.22	0.02	0.37
GGA $+$ SOC $+ U$	3.93	0	3.79	5.89	11.98	−0.43	−0.67	0.02	0.65

FIG. 7. Order parameter (solid line and left axis) and specific heat (dashed line and right axis) of Na_4IrO_4 calculated as a function of temperature on the basis of the classical spin Hamiltonian without SIA (red curves) and with SIA (green curves).

specific heat at a given temperature T. As shown in Fig. 7, without considering the SIA, the order parameter and the specific heat give similar results. The critical temperature T_N is 28 K, evaluated from the peak position of the specific heat or from the values where the order parameter becomes negligible. The critical temperature as well as the height of the specific heat peak increase upon including SIA in the MC simulations. The value of T_N increases to 57 K, similar to the case in another infinite-layer oxide $SrFeO_2$ with square planar coordination, where the critical temperature also increases when adding the magnetic anisotropy energy [21]. The magnetism is always collinear in Na_4IrO_4, considering the SIA, the spin moments being along the c axis perpendicular to the IrO_4 square plane. In both cases, Na_4IrO_4 relaxes to the same AFM2 magnetic ground state with FM ab planes, antiferromagnetically coupled out of plane, corresponding to an antiparallel alignment of the spin magnetic moment of two Ir atoms in the crystallographic unit cell, revealed by first-principles calculations to be the lowest-energy magnetic state.

IV. CONCLUSIONS

In summary, the square planar coordination of IrO_4 plaquettes plays a crucial role in the electronic structure and magnetic properties of Na_4IrO_4, as shown by our comprehensive DFT calculations joint with MC simulations. The unusual square planar crystal field and the strong hybridization effects give rise to an intermediate-spin state and an insulating electronic structure, robust against different magnetic ordering states, Coulomb parameters, and even relativistic interactions. SOC produces a large MCA with an easy axis along the c axis perpendicular to the IrO_4 square plane. When spin-exchange interactions are evaluated by total energy calculations and mapping analysis, quite weak AFM interactions are obtained, consistent with the picture of rather isolated IrO_4 units. Moreover, MC simulations predict a quite low Néel temperature, consistent with experiments, and a collinear long-range AFM magnetic ground state. We hope our theoretical simulations will stimulate experimental works aimed at detailed magnetic property measurements and characterizations, to further understand the magnetic ground state and exploit the large anisotropy of the uncommon square planar coordinated Na_4IrO_4.

Note added. Recently, we became aware of Ref. [54] where a similar first-principles study was performed for the square planar coordinated Na_4IrO_4 discussed here. The calculated magnetic ground state and the spin-exchange interactions, as well as the predicted giant magnetocrystalline anisotropy, in the present work are all consistent with the main conclusions in Ref. [54] although they used a full electron method in the local density approximation while we used a plane-wave method in the generalized gradient approximation.

[1] D. Pesin and L. Balents, Nat. Phys. **6**, 376 (2010).

[2] W. Witczak-Krempa, G. Chen, Y. B. Kim, and L. Balents, Annu. Rev. Condens. Matter Phys. **5**, 57 (2014).

[3] J. G. Rau, E. K. H. Lee, and H. Y. Kee, Annu. Rev. Condens. Matter Phys. **7**, 195 (2016).

[4] Y. Chen, Y.-M. Lu, and H. Y. Kee, Nat. Commun. **6**, 6593 (2015).

[5] B. J. Kim, H. Jin, S. J. Moon, J.-Y. Kim, B.-G. Park, C. S. Leem, J. Yu, T. W. Noh, C. Kim, S.-J. Oh, J.-H. Park, V. Durairaj, G. Cao, and E. Rotenberg, Phys. Rev. Lett. **101**, 076402 (2008).

[6] B. J. Kim, H. Ohsumi, T. Komesu, S. Sakai, T. Morita, H. Takagi, and T. Arima, Science **323**, 1329 (2009).

[7] K. Mader and R. Hoppe. Z. Anorg. Allg. Chem. **619**, 1647 (1993).

[8] S. Kanungo, B. Yan, P. Merz, C. Felser, and M. Jansen, Angew. Chem., Int. Ed. **54**, 5417 (2015).

[9] N. P. Armitage, P. Fournier, and R. L. Greene. Rev. Mod. Phys. **82**, 2421 (2010).

[10] Y. Tsujimoto, C. Tassel, N. Hayashi, T. Watanabe, H. Kageyama, K. Yoshimura, M. Takano, M. Ceretti, C. Ritter, and W. Paulus, Nature **450**, 1062 (2007).

[11] G. A. Petrakovskii, K. A. Sablina, D. A. Velikanov, A. M. Vorotynov, N. V. Volkov, and A. F. Bovina, Crystallogr. Rep. **45**, 853 (2000).

[12] J. N. Hancock, G. Chabot-Couture, Y. Li, G. A. Petrakovskiĭ, K. Ishii, I. Jarrige, J. Mizuki, T. P. Devereaux, and M. Greven, Phys. Rev. B **80**, 092509 (2009).

[13] M. Saito, K. Ishikawa, K. Taniguchi, and T. Arima, Phys. Rev. Lett. **101**, 117402 (2008).

[14] G. Kresse and J. Furthmüller, Phys. Rev. B **54**, 11169 (1996).

[15] P. E. Blöchl, Phys. Rev. B **50**, 17953 (1994).

[16] G. Kresse and D. Joubert, Phys. Rev. B **59**, 1758 (1999).

[17] J. P. Perdew, K. Burke, and M. Ernzerhof, Phys. Rev. Lett. **77**, 3865 (1996).

[18] A. I. Liechtenstein, V. I. Anisimov, and J. Zaanen, Phys. Rev. B **52**, R5467 (1995).

[19] M. Rahman, Y.-z. Nie, and G.-h. Guo, Inorg. Chem. **52**, 12529 (2013).

[20] C. Tassel and H. Kageyama, Chem. Soc. Rev. **41**, 2025 (2012).

[21] H. J. Xiang, S. H. Wei, and M. H. Whangbo, Phys. Rev. Lett. **100**, 167207 (2008).

[22] J. M. Pruneda, J. Íñiguez, E. Canadell, H. Kageyama, and M. Takano, Phys. Rev. B **78**, 115101 (2008).

[23] H. Jin, H. Jeong, T. Ozaki, and J. Yu, Phys. Rev. B **80**, 075112 (2009).

[24] X. Wan, A. M. Turner, A. Vishwanath, and S. Y. Savrasov, Phys. Rev. B **83**, 205101 (2011).

[25] A. E. Taylor, S. Calder, R. Morrow, H. L. Feng, M. H. Upton, M. D. Lumsden, K. Yamaura, P. M. Woodward, and A. D. Christianson, Phys. Rev. Lett. **118**, 207202 (2017).

[26] Y Du, X. Wan, L. Sheng, J. Dong, and S. Y. Savrasov, Phys. Rev. B **85**, 174424 (2012).

[27] M.-C. Jung, Y.-J. Song, K.-W. Lee, and W. E. Pickett, Phys. Rev. B **87**, 115119 (2013).

[28] S. Calder, J. H. Lee, M. B. Stone, M. D. Lumsden, J. C. Lang, M. Feygenson, Z. Zhao, J.-Q. Yan, Y. G. Shi, Y. S. Sun, Y. Tsujimoto, K. Yamaura, and A. D. Christianson, Nat. Commun. **6**, 8916 (2014).

[29] K. S. Pedersen, J. Bendix, A. Tressaud, E. Durand, H. Weihe, Z. Salman, T. J. Morsing, D. N. Woodruff, Y. Lan, W. Wernsdorfer, C. Mathonière, S. Piligkos, S. I. Klokishner, S. Ostrovsky, K. Ollefs, F. Wilhelm, A. Rogalev, and R. Clérac, Nat. Commun. **7**, 12195 (2016).

[30] G. Cao, T. F. Qi, L. Li, J. Terzic, S. J. Yuan, L. E. DeLong, G. Murthy, and R. K. Kaul, Phys. Rev. Lett. **112**, 056402 (2014).

[31] S. Bhowal, S. Baidya, I. Dasgupta, and T. Saha-Dasgupta, Phys. Rev. B **92**, 121113 (2015).

[32] H. Zhang, K. Haule, and D. Vanderbilt, Phys. Rev. Lett. **111**, 246402 (2013).

[33] S.-W. Kim, C. Liu, H.-J. Kim, J.-H. Lee, Y. Yao, K.-M. Ho, and J.-H. Cho, Phys. Rev. Lett. **115**, 096401 (2015).

[34] C. Donnerer, Z. Feng, J. G. Vale, S. N. Andreev, I. V. Solovyev, E. C. Hunter, M. Hanfland, R. S. Perry, H. M. Rønnow, M. I. McMahon, V. V. Mazurenko, and D. F. McMorrow, Phys. Rev. B **93**, 174118 (2016).

[35] S. Moser, L. Moreschini, A. Ebrahimi, B. Dalla Piazza, M. Isobe, H. Okabe, J. Akimitsu, V. V. Mazurenko, K. S. Kim, A. Bostwick, E. Rotenberg, J. Chang, H. M. Rønnow, and M. Grioni, New J. Phys. **16**, 013008 (2014).

[36] J. K. Kawasaki, M. Uchida, H. Paik, D. G. Schlom, and K. M. Shen, Phys. Rev. B **94**, 121104 (2016).

[37] X. Wang, R. Wu, D.-s. Wang, and A. J. Freeman, Phys. Rev. B **54**, 61 (1996).

[38] H. Xiang, C. Lee, H. J. Koo, X. Gong, and M. H. Whangbo, Dalton Trans. **42**, 823 (2013).

[39] D. Dai, H. Xiang, and M. H. Whangbo, J. Comput. Chem. **29**, 2187 (2008).

[40] M. H. Whangbo, E. E. Gordon, H. Xiang, H. J. Koo, and C. Lee, Acc. Chem. Res. **48**, 3080 (2015).

[41] P. Bruno, Phys. Rev. B **39**, 865 (1989).

[42] H. Takayama, K. Bohnen, and P. Fulde, Phys. Rev. B **14**, 2287 (1976).

[43] E. E. Gordon, H. Xiang, J. Köhler, and M. H. Whangbo, J. Chem. Phys. **144**, 114706 (2016).

[44] S. Ayaz Khan, P. Blaha, H. Ebert, J. Minár, and O. Šipr, Phys. Rev. B **94**, 144436 (2016).

[45] N. A. Bogdanov, R. Maurice, I. Rousochatzakis, J. van den Brink, and L. Hozoi, Phys. Rev. Lett. **110**, 127206 (2013).

[46] M. A. Laguna-Marco, P. Kayser, J. A. Alonso, M. J. Martínez-Lope, M. van Veenendaal, Y. Choi, and D. Haskel, Phys. Rev. B **91**, 214433 (2015).

[47] L. S. I. Veiga, G. Fabbris, M. van Veenendaal, N. M. Souza-Neto, H. L. Feng, K. Yamaura, and D. Haskel, Phys. Rev. B **91**, 235135 (2015).

[48] A. E. Taylor, R. Morrow, R. S. Fishman, S. Calder, A. I. Kolesnikov, M. D. Lumsden, P. M. Woodward, and A. D. Christianson, Phys. Rev. B **93**, 220408(R) (2016).

[49] C. Autieri and B. Sanyal, New J. Phys. **16**, 113031 (2014).

[50] L. Noodleman, J. Chem. Phys. **74**, 5737 (1981).

[51] L. Noodleman and E. R. Davidson, Chem. Phys. **109**, 131 (1986).

[52] L. Noodleman and D. A. Case, Adv. Inorg. Chem. **38**, 423 (1992).

[53] B. Skubic, J. Hellsvik, L. Nordström, and O. Eriksson, J. Phys.: Condens. Matter **20**, 315203 (2008).

[54] D. Wang, F. Tang, Y. Du, and X. Wan, Phys. Rev. B **96**, 205159 (2017).